Optimal estimation retrieval of tropospheric ammonia from the Geostationary Interferometric Infrared Sounder onboard FengYun-4B

Zhao-Cheng Zeng[1,*], Lu Lee[2], Chengli Qi[2]

[1]School of Earth and Space Sciences, Peking University, Beijing 100871, China
5 [2]Innovation Center for FengYun Meteorological Satellite, Key Laboratory of Radiometric Calibration and Validation for Environmental Satellites, National Satellite Meteorological Center, China Meteorological Administration, Beijing 100081, China

*Correspondence to: Z.-C. Zeng (zczeng@pku.edu.cn)

Abstract. Atmospheric ammonia (NH_3) is a reactive nitrogen compound that pollutes our environment and threatens public health. Monitoring the spatial and temporal variations is important for quantifying its emissions and depositions and evaluating the 10 strategies for managing anthropogenic sources of NH_3. In this study, we present an NH_3 retrieval algorithm based on the optimal estimation method for the Geostationary Interferometric Infrared Sounder (GIIRS) onboard China's FengYun-4B satellite (FY-4B/GIIRS). In particular, we examine the information content based on the degree of freedom for signal (DOFS) in retrieving the diurnal NH_3 in East Asia, with a focus on two source regions including North China Plain and North India. Different from previous studies, our retrievals are implemented using two different absorption micro-windows (920-940 cm^{-1} and 955-975 cm^{-1}), and their 15 difference in retrievals is used to imply the impact of spectral noise on the retrieval uncertainty. Retrieval results using FY-4B/GIIRS spectra from July to December 2022 show that the two retrieval sets using different micro-windows are highly consistent, with a correlation coefficient of 0.81 and a root-mean-square-error of 3.2×10^{15} molec/cm^2 when DOFS>0.5. no large systematic bias is observed. The DOFS for the majority ranges from 0 to 1.0, mainly depending on the thermal contrast (TC) defined as the temperature difference between the surface and the lower atmosphere. Consistent with retrievals from low-earth-orbit (LEO) 20 infrared sounders, the detection sensitivity, as quantified by the averaging kernel (AK) matrix, peaks in the lowest 2 km atmospheric layers. The DOFS and TC are highly correlated, resulting in a typical "butterfly" shape. That is, the DOFS increases when TC becomes either more positive or more negative. The NH_3 columns from FY-4B/GIIRS show a significant diurnal cycle in summer (July-August) in North China Plain, in good agreement with the day-night gradient from the collocating IASI retrievals. The weak and moderate diurnal cycles in September-October and November-December, respectively, are also presented from both 25 FY-4B/GIIRS and IASI retrievals. This study demonstrates the capability of FY-4B/GIIRS in capturing the diurnal NH_3 changes in East Asia, which will have the potential to improve regional and global air quality and climate research.

1. Introduction

Atmospheric ammonia (NH_3) is a reactive nitrogen compound that plays an important role in the global nitrogen cycle (**Galloway et al. 2004**). Its emissions to the atmosphere are destined to increase in the coming decades primarily driven by agriculture 30 emissions coming from the excess use of nitrogen fertilizers (**Fowler et al., 2013**). Changes in NH_3 emissions have many negative environmental impacts, including the loss of biodiversity (**Erisman et al., 2013**), the eutrophication of water bodies and the acidification of terrestrial ecosystems (**Paerl et al., 2014**), the degradation of air quality caused by the production of ammonium containing aerosols (**Seinfeld and Pandis, 2006**), and the change in radiative forcing that affect global and local climate (**Abbatt et al., 2006; Isaksen et al., 2009**). Monitoring the spatial distribution and temporal variations of atmospheric NH_3 is therefore 35 important for quantifying NH_3's emissions and depositions and evaluating the strategies for managing anthropogenic sources of NH_3.

Atmospheric
Measurement
Techniques
Discussions

Open Access
EGU

Over the past decade, space-borne observations of NH_3 have provided measurements with daily global coverage that greatly improve our understanding of the sources, depositions, and variabilities of NH_3 (e.g., **Zhu et al., 2015; Warner et al., 2017; Van Damme et al., 2021**). The capability of using an infrared hyperspectral sounder to detect NH_3 was first demonstrated using

40   observations from the Tropospheric Emission Spectrometer (TES; **Beer et al., 2008; Shephard et al., 2011**) and the Infrared Atmospheric Sounding Interferometer (IASI; **Clarisse et al., 2009, 2010; Coheur et al., 2009**). Currently, long-term measurements of NH_3 are available from IASI (**Van Damme et al., 2021**), the Cross-track Infrared Sounder (CrIS; **Shephard et al., 2020**), the Atmospheric Infrared Sounder (AIRS; **Warner et al., 2016**), and the Thermal and Near-infrared Spectrometer for Observation-Fourier Transform Spectrometer (TANSO- FTS; **Someya et al., 2020**). However, the above-mentioned polar-orbiting satellites

45   can only make up to two overpass measurements each day over the same location. The diurnal cycle of NH_3 is therefore under-constrained from polar-orbit observations. Since NH_3 is a highly reactive compound, it has a relatively short lifetime ranging from a few hours to days (**Aneja et al., 2001**). As a result, NH_3 presents a large spatial heterogeneity and temporal variability. The important information on the diurnal cycle is therefore critical to constrain the emission, deposition, and transport processes of NH_3 and the role of meteorological conditions in driving these processes.

50   The Geostationary Interferometric Infrared Sounder (GIIRS) onboard the FengYun-4B satellite was launched in 2021 with improved sensitivity over its predecessor FY-4A/GIIRS launched in 2016 (**Yang et al., 2017**). GIIRS was designed to probe the three-dimension water vapor and temperature profiles for weather forecast purposes. With its high spectral resolution (0.625 cm^{-1}) and sensitivity comparable to current low-earth-orbit (LEO) satellites, FY-4B/GIIRS is suited for detecting the changes of various atmospheric trace gases (e.g., **Zeng et al., 2022**). The strength of using FY-4B/GIIRS lies in its capability to scan East Asia every

55   two hours with a spatial resolution of 12 km, offering a unique opportunity to constrain the diurnal cycles of critical atmospheric composition at high spatial resolution. The application of GIIRS in detecting NH_3 has been successfully demonstrated using spectra collected by FY-4A based on an IASI retrieval method (**Clarisse et al., 2021**). The study showed that the unprecedented temporal sampling of GIIRS enables the measurement of diurnal and nocturnal variations of NH_3. Since the retrieval method used in **Clarisse et al. (2021)** is based on hyperspectral radiance index (HRI) and a trained neural network that relates HRI to NH_3 columns

60   (**Whitburn et al., 2016**), information content analysis for the GIIRS spectra was not fully investigated.

Optimal estimation method (**Rodgers, 2020**) that enables information content analysis has been applied in previous studies on retrieving NH_3 from space (**Clarisse et al., 2009, 2010; Shephard et al., 2011; Warner et al., 2016, Shephard et al., 2011,2015; Someya et al., 2020**). It was found that the information available from the infrared sounder spectra for quantifying NH_3, especially its abundance in the PBL, strongly depends on the thermal contrast (TC), which is defined as the temperature difference between

65   the surface skin and the lower atmosphere. Because of its short lifetime, NH_3 is mostly concentrated in the planetary boundary layer (PBL) and the peak sensitivity of NH_3 detection from an infrared sounder is also found to be close to the surface. Previous studies (e.g., **Clarisse et al., 2010**) concluded that the TC and its abundance are two important factors that determine the information content of $NH3$ detection from the infrared spectra. In general, higher NH_3 concentrations and larger TC result in a more accurate estimate of NH_3 from space-borne measurements.

70   In this study, we applied the FY-GeoAIR retrieval algorithm developed by the group (**Zeng et al., 2022**) based on the optical estimation theory to retrieve NH_3 from FY-4B/GIIRS. The retrieval algorithm uses the absorption feature of NH3's v_2 rotational-vibrational band centered around 10.5 μm (~950 cm^{-1}). The primary goals are to quantify the information content of FY-4B/GIIRS observations in constraining the diurnal cycle of NH_3 columns and the impact of TC on the retrieval accuracy. Different from previous studies, our retrievals are implemented using two different absorption micro-windows (920-940 cm^{-1} and 955-975 cm^{-1})

75   that contain strong NH_3 absorption feature, and their difference in retrievals is used to imply the impact of spectral noise on the retrieval uncertainty.

Atmospheric
Measurement
Techniques
Discussions

This remaining paper is organized as follows. The FY-4B/GIIRS observation mode and the collected spectra are introduced in **Section 2**; In **Section 3**, the FY-GeoAIR algorithm for NH_3 retrieval is described; The retrieval results and information content analysis are presented in **Section 4**, followed by discussions in **Section 5** and conclusions in **Section 6**.

2. GIIRS onboard FengYun-4B

80   FY-4B/GIIRS is an infrared Fourier transform spectrometer based on a Michelson interferometer located at an altitude of 35,786 km above the equator at 133°E. The primary goal is to probe the three-dimensional atmospheric structure of temperature and water vapor over east Asia for improving numerical weather forecast. **Figure 1(b)** shows the coverage of FY-4B/GIIRS over East Asia and part of South Asia and Southeast Asia in one measurement cycle which lasts 2-hour. In each cycle, GIIRS makes 12 horizontal

85   scans from north to south. Each scan sequence consists of 27 fields-of-regards (FORs) from west to east that collects upwelling infrared radiation of Earth scenes (ESs), followed by one deep space (DS) and one internal calibration target (ICT) measurement for ES radiometric calibration. For each FOR, a 2-dimension infrared plane array detector, containing 16×8 pixels with a sparse arrangement, conducts the measurement over the target region. The starting hours for the 12 measurement cycles in a day were 0, 2, 4, …, 22h UTC, respectively, and have been changed to 1, 3, 5, …, 23h UTC, respectively, after September 06, 2022. The

90   observation domain, as shown in **Figure 1(a)**, covers the two important NH_3 emission source regions in Asia: The North China Plain and North India. The FY-4B/GIIRS observed spectra include a long-wave infrared band from 680 to 1130 cm^{-1} and a mid-wave infrared band from 1650 to 2250 cm^{-1} with a uniform spectral resolution of 0.625 cm^{-1}. With low instrument noise and a high spectral resolution similar to current LEO infrared sounders, GIIRS is in principle capable of measuring trace gases, including NH_3, and providing full day-night diurnal cycle observations. The spatial footprint size of each pixel on the Earth's surface is about 12

95   km at Nadir, which is an improvement over FY-4A/GIIRS (16 km). **Fig. 1(c)** shows an example of GIIRS spectra in the long-wave band. Post-launch assessment of the radiometric performances of FY-4B/GIIRS using a series of blackbody calibration experiments showed that the noise equivalent differential radiance (NedR) on average in the long-wave infrared 900-1000 cm^{-1} bands, covering the NH_3 absorption channel, is about 0.1 $mW/(m^2 \cdot sr \cdot cm^{-1})$. The corresponding noise equivalent differential temperature (NedT) on average is about 0.1 K@280K blackbody. The low instrument noise for FY-4B/GIIRS, comparable to existing infrared sounders,

100   makes it possible to provide strong constrain on measuring the diurnal change of NH_3 column.
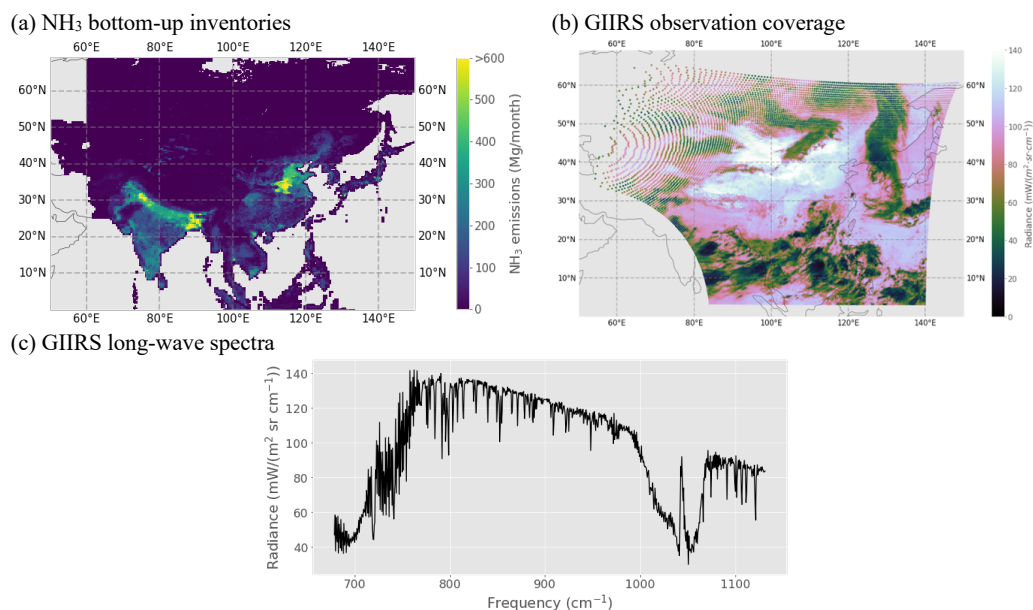
Figure 1. (a) Bottom-up NH₃ emissions averaged from July to December of 2010. These are the total amount combining emissions from agricultural, industrial, power plant, residential, and transportation sectors. This emission inventory is adopted from MIX dataset (Li et al., 2017); (b) The GIIRS observation coverage is color-shaded using the observed radiance at 900 cm^{-1} from FY-4B/GIIRS. This example is adopted from the measurement cycle (hours 12-13 in Beijing Time) on July 07, 2022; (c) Example of FY-4B/GIIRS measured long-wave spectra, which covers the NH₃ absorption band centered around 950 cm^{-1}.

3. The FY-GeoAIR retrieval algorithm for NH₃

The FengYun Geostationary satellite Atmospheric Infrared Retrieval (FY-GeoAIR) algorithm was originally developed for retrieving carbon monoxide from FY-4B/GIIRS spectra. The algorithm combines a forward radiative transfer model to simulate upwelling thermal radiation and an optimal estimation-based inverse model to retrieve trace gases and auxiliary parameters from the observed spectra. Here, a brief introduction to FY-GeoAIR is given with descriptions of changes needed to adapt it to NH₃ retrieval. More details about the FY-GeoAIR retrieval algorithm can be referred to **Zeng et al. (2022)**.

3.1 The Forward radiative transfer model for simulating observed spectra

An accurate radiative transfer (RT) model is an important component in the inversion system for simulating upwelling thermal radiation that would be observed by FY-4B/GIIRS when given the relevant atmospheric, surface, and instrumental parameters as inputs. The upwelling spectral radiance is computed following the radiative transfer theory for thermal radiation that has been described in **Clough et al. (2006)** and **Hurtmans et al. (2012)**. Under clear sky conditions, scattering by clouds and aerosols can be ignored. The upwelling radiance received by FY-4B/GIIRS can be accurately approximated by the sum of four main components, including the upwelling surface emission, the upwelling atmospheric emission integrated from the bottom- to the top of the atmosphere, the surface-reflected downwelling atmospheric emission, and the surface-reflected solar radiation. Although the last component is very small in the long-wave band, it is added here for completeness. The two different absorption micro-windows
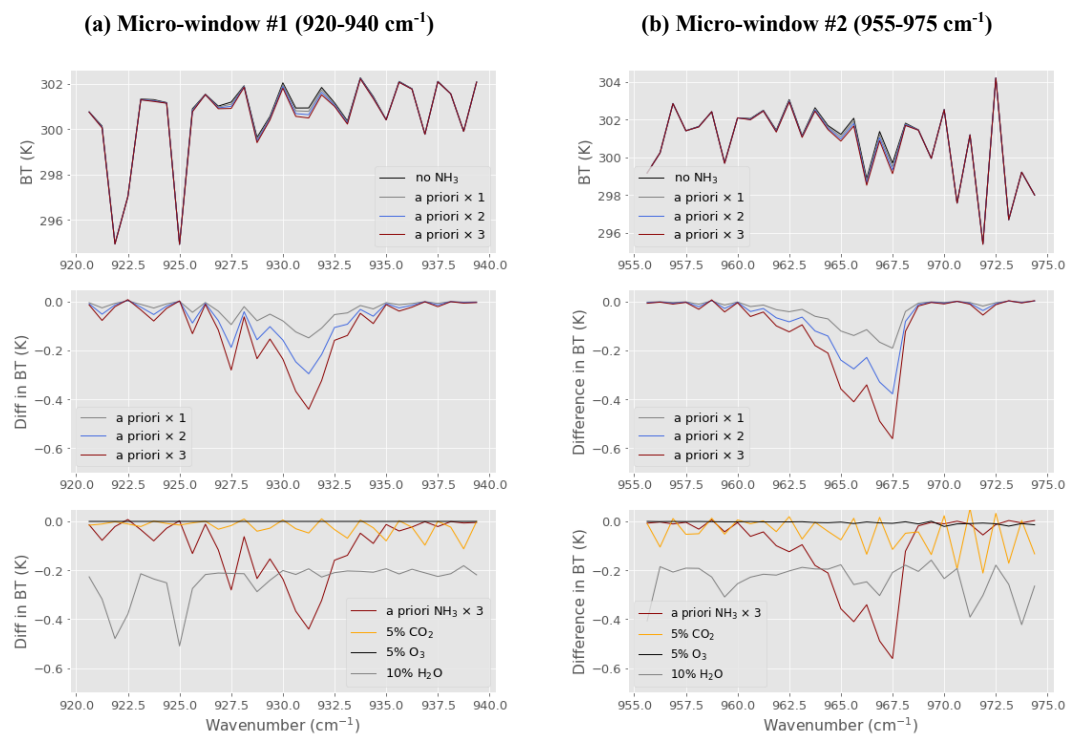
(920-940 cm^{-1} and 955-975 cm^{-1}) used for retrieval are shown in **Figure 2**. The micro-windows contain strong NH₃ absorption features that are distinguishable from interference gases.

125   The atmospheric, surface and instrumental parameters to drive the forward model are adopted from various sources. These parameters are the atmospheric state such as the profiles of temperature, water vapor, and atmospheric composition, the surface parameters such as the surface emissivity, and the instrumental specifications such as instrument spectral response function and observing geometries. Specifically, the atmospheric temperature data are extracted from ECMWF ERA5 reanalysis (**Hersbach et al., 2020**); For the interference gases, H_2O and O_3 are extracted from ECMWF ERA5 reanalysis (**Hersbach et al., 2020**); N_2O and

130   CO_2 are extracted from ECMWF CAMS global inversion-optimized greenhouse gas fluxes and concentrations (**ECMWF, 2022**); For the surface land data, we used the global infrared land surface emissivity database from the University of Wisconsin-Madison (UOW-M) (**Seemann et al., 2007**); Surface skin temperature and surface pressure are extracted from ERA5 hourly data on single level (**Hersbach et al., 2020**). The absorption coefficient look-up tables for calculating gas absorption are built using the extensively validated Line-By-Line Radiative Transfer Model (LBLRTM v12.11; **Clough et al., 2005**). Since the NH_3 is more

135   concentrated in the PBL compared to carbon monoxide, we therefore only retrieve the layers below 200 hPa by equally separating them into layers with 1 km thickness, except the bottom layer which is also determined by the surface pressure. The number of layers for retrieval ranges from 7 (at high altitude) to 11 layers (at low altitude).

(a) Micro-window #1 (920-940 cm^{-1})   **(b) Micro-window #2 (955-975 cm^{-1})**

Figure 2. The characterizations of the two micro-windows used for FY-4B/GIIRS NH₃ retrieval (a) 920-940 cm^{-1} and (b)

140   **955-975 cm^{-1}. The micro-windows cover two strong absorption features of the NH₃ ν_2 vibrational-rotational band centered around 950 cm^{-1}. The upper panels show the comparison of simulated spectra using the forward model with three different NH₃ concentrations based on the a priori NH₃ profiles shown in Figure 3; The middle panels show their differences relative to the baseline without NH₃; The lower panels show the absorption difference between NH₃ and the interference gases.**

3.2 The Retrieval algorithm in FY-GeoAIR based on optimal estimation theory

145 The goal of the retrieval algorithm for retrieving NH_3 from FY-4B/GIIRS based on optimal estimation theory is to find a solution for the state vector, which consists of NH_3 profile and auxiliary parameters, such that the simulated spectra from the RT forward model best fit the measured spectra. The auxiliary parameters include H_2O profile, scale factors for the columns of the remaining interference gases, surface skin temperature, and scale factor for the atmospheric temperature profile. The solution from the retrieval algorithm is the state vector which maximize the a posteriori probability given the FY-4B/GIIRS spectra. The Levenberg-

150 Marquardt modification of the Gauss-Newton method is used to search the solution. The optimal estimation method has been described thoroughly in **Rodgers (2000)** and applied in several previous studies by the group (**Zeng et al., 2017; Zeng et al., 2021; Natraj et al., 2022; Zeng et al., 2022**).

Two important metrics from optical estimation method for interpreting the retrieval results are the DOFS and Averaging Kernel (AK) matrix. AK matrix is a metric that quantifies the sensitivity of the retrieval to the true state by the observing system. The full

155 AK matrix ($m \times m$) is given by:

$$\mathbf{A} = (\mathbf{K}^T \mathbf{S}_\varepsilon^{-1} \mathbf{K} + \mathbf{S}_a^{-1})^{-1} \mathbf{K}^T \mathbf{S}_\varepsilon^{-1} \mathbf{K} \qquad (1)$$

where A_{ij} represents the derivative of the NH_3 retrieval at level i with respect to the NH_3 truth at level j; The matrix dimension m is the number of atmospheric layers; $\mathbf{K}$ is the Jacobian matrix, which is the first derivative of the forward model with respect to the state vector; $\mathbf{S}_a$ is the *a priori* covariance matrix for the state vector; $\mathbf{S}_\varepsilon$ is the measurement error covariance matrix. Noted that

160 similar to the CO retrieval algorithm (**Zeng et al., 2022**), we have enlarged the spectra noise by 2.0 times such that the averaged reduced χ^2 value from the optimal estimation NH_3 retrieval is close to 1.0. This extra noise represents the unaccounted uncertainty from the forward model and absorption spectroscopy by the original instrument noise alone.

A "perfect" observing system, which has sufficiently good sensitivity to each element in the retrieval vector, would have an AK matrix close to an identity matrix by theory. In reality, the detectivity is limited by various factors including the spectra noise, a

165 priori uncertainty, and the sensitivity of the spectra to the geophysical variables in the state vector. As a result, the AK can be very different from an identity matrix. In general, the information from the true state is smoothed vertically over different layers by the retrieval algorithm. In this case, the rows of AK represent the smoothing functions. As described in **Rodgers (2020)**, the trace of the AK matrix is defined as the DOFS, which represents the number of independent elements of information extracted from the spectra by the retrieval algorithm for constraining NH_3. DOFS is an important metric that quantify the vertical resolution of the

170 retrieval profile. For example, a DOFS of 1.0 means that at least one independent piece of information can be retrieved from the spectral measurement to constrain the vertical distribution of NH_3.

3.3 The a priori NH_3 profile and covariance matrix

A fixed a priori is preferred for the purpose of this study for two reasons: (1) a fixed a priori makes the interpretation of the results easier compared to a time varying a priori. Any changes seen in the spatial and temporal patterns in NH_3 relative to the a priori

175 reflects the information gained from the FY-4B/GIIRS spectra; (2) it is not applicable to get a reasonable a priori estimate for all hours in a day from just the spectra (e.g., using channel brightness temperature difference as in **Shephard et al. (2011)** and **Warner et al. (2016)**) without relying on model simulations, because the diurnal change of TC that affects GEO satellite observation is much more complex than that in the two overpasses for LEO satellite each day. The NH_3 profile, as shown in **Figure 3**, for the retrieval algorithm is derived from NH_3 simulations from the Goddard Earth Observing System composition forecast (GEOS-CF;

180 **Keller et al., 2021**) model developed by NASA's Global Modeling and Assimilation Office (GMAO). One year of measurements in 2022 is used to get the mean and standard deviation of NH_3 vertical distribution. To avoid over sampling of the background

regions, only simulations in the representative land regions in east Asia (20°-60°N and 110°-120°E) and south Asia (20°-40°N and 70°-100°E) are used.
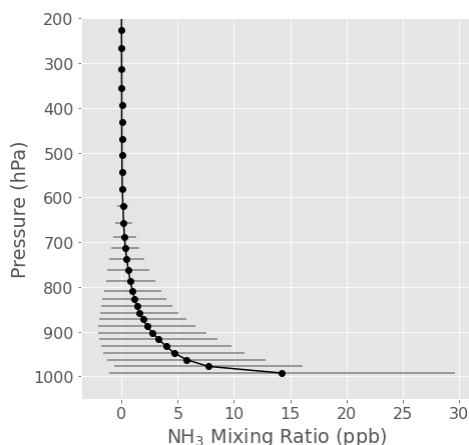
185   **Figure 3. The a priori NH₃ profile used for retrievals of NH₃ in the FY-GeoAIR algorithm for FY-4B/GIIRS. This profile is computed from the GEOS-CF NH₃ simulations (Keller et al., 2021) in 2022 in representative land regions in east Asia (20°-60°N and 110°-120°E) and south Asia (20°-40°N and 70°-100°E). The error bars represent one standard deviation for different layers from all NH₃ profiles.**

190   **3.4 Post-filtering of NH₃ retrievals**

All cloud-screened FY-4B/GIIRS spectra acquired over land with a solar zenith angle less than 70° are used in the retrieval. To filter out cloudy pixels, we use the higher-resolution (4 km) level-2 cloud mask (CLM) data product from the Advanced Geostationary Radiation Imager (AGRI) onboard FY-4B. After cloud screening, there are in total of 11.7 million clear-sky data points for the 6 months from July to December of 2022. In the post-processing, multiple filters are applied to ensure good retrieval
195   quality. First, retrievals that fail to converge after 10 iterations are excluded. Second, retrievals with the goodness of fit, quantified by reduced χ^2, less than 1.5 are excluded. Lastly, retrievals with RMSE of fitting residual larger than 0.25 K are excluded. After post-filtering, about 9.5 million data points pass the filters. The histograms of the reduced χ^2 and spectral fitting residual are shown in **Supplementary Figure S1**. The average reduced χ^2 after post-filtering is 0.86 for micro-window #1 and 0.76 for micro-window #2, suggesting satisfying goodness of fit. In the following analysis, two extra filters may apply, including the DOFS used to exclude
200   data that do not have enough constrain from the observed spectra and the difference of retrieval using the two different micro-windows to exclude data with large uncertainty that are caused by high spectra noise.

4. Results of NH$_3$ retrievals from FY-4B/GIIRS

4.1 Comparison of NH$_3$ retrievals using the two different micro-windows

205   As shown in **Figure 2**, the two micro-windows (920-940 cm^{-1} and 955-975 cm^{-1}) originated from the NH$_3$ v_2 rotational-vibrational transitions have similar absorption characteristics, including the absorption structure and sensitivity. Theoretically, applying the FY-GeoAIR algorithm using these two micro-windows should produce similar NH$_3$ retrievals. However, due to the impact of spectral noise, which is assumed to be close to random, the retrieval results are expected to show a discrepancy. In addition, the slight difference in their absorption structures and sensitivities, with micro-window #2 presenting a stronger absorption and

210 therefore higher sensitivity than micro-window #1, may contribute to the discrepancy. As shown in **Figure 4(a)**, the DOFSs show high consistencies, with a correlation coefficient of 0.97, suggesting the two micro-windows contain similar information in capturing the NH$_3$ variabilities. We do observe a slightly higher DOFS for micro-window #2 resulting from its stronger absorption and sensitivity. In **Figure 4(b),** the retrieved NH$_3$ columns are compared for retrievals with DOFS larger than 0.5, a threshold used to remove retrievals that gain weak constrain from the FY-4B/GIIRS spectra. The correlation coefficient between the two datasets

215 is 0.81 with a root-mean-square-error of 3.2×10^{15} molec/cm^2. Fortunately, no large systematic bias is observed, indicating the small difference in absorption structure and sensitivity in the micro-windows are not causing bias in the retrievals. The difference is primarily caused by spectral noise. Therefore, the difference serves as a good indicator of the impact of spectra noise on the retrieval and can be used as a post-filtering criterion to obtain retrievals with high accuracy.
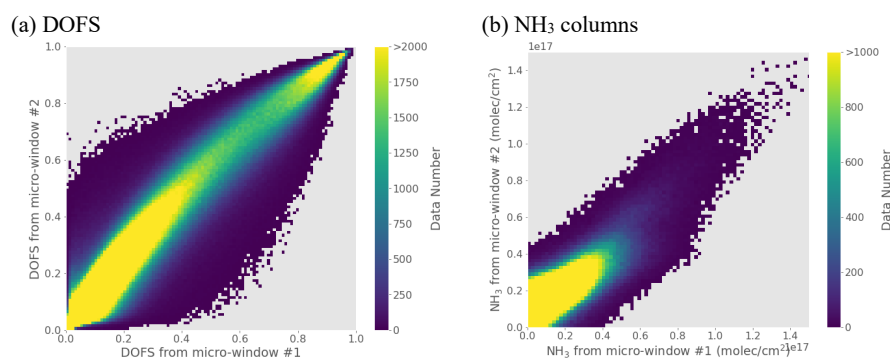
220 **Figure 4. The comparison of NH$_3$ retrievals using micro-window #1 (920-940 cm^{-1}) and micro-window #2 (955-975 cm^{-1}): (a) the DOFS, which shows a correlation coefficient of 0.97 for a total of 11.7 million data points, and (b) the retrieved NH3 columns. For the comparison of columns, retrievals have been filtered by DOFS>0.5. In total, 1.6 million data points pass the filter. The correlation coefficient between the two column datasets is 0.81 with a root-mean-square-error of 3.2×10^{15} molec/cm^2.**

225 ### 4.2 Information content analysis based on DOFS and AK matrix

     This section conducted information content analysis by investigating the spatial and diurnal changes of DOFS from NH$_3$ retrievals, and how the DOFS changes are related to TC. In addition, we examine the diurnal changes of the vertical sensitivity as quantified by AK matrix. In particular, we focus on three representative regions including source regions in North China Plain and North India and non-source region in Mongolia.

230   The spatial maps of DOFS, as shown in **Figure 5**, for different times in a day clearly show the spatial gradient and diurnal change. In July and October, the DOFSs in the afternoon is usually the highest and those in the evening the lowest. In December, night-time DOFS are significantly higher than other seasons. Previous studies by **Clarisse et al. (2010)** and **Bauduin et al. (2017)**

using IASI observations have shown that the detectivity quantified by DOFS is primarily driven by the change of TC. When TC is more positive, more thermal infrared radiation are emitting from the surface, the observed spectra will show more robust absorption features and therefore higher detectivity. On the other hand, when TC is more negative, suggesting the atmosphere is warmer than the surface and therefore can be distinguished more easily, the observed spectra will show more robust emission features that increases detectivity. In addition, higher concentration of target gases provides stronger detectivity than lower concentration. The relationships between TC and DOFS are illustrated in **Figure 6** for the three representative regions: North China Plain, North India and Mongolia. A typical "butterfly" shape can be seen in almost all cases. In general, the DOFS increases when the TC becomes either more positive or more negative, consistent with results from **Clarisse et al. (2010)** and **Bauduin et al. (2017)** based on polar-orbiting satellite. In NH_3 source regions (North China Plain and North India), the DOFSs are higher for the same TC compared with non-source region (Mongolia), suggesting the contribution from higher NH_3 concentration to the detectivity.

This strong correlations between DOFS and TC or concentration is also reflected in the spatial maps of DOFSs in **Figure 5** when analyzed with the corresponding TC maps in the **Supplementary Figure S2**. The source regions in North China Plain and North India have higher DOFSs than other non-source regions. For the same region (e.g., North China Plain), the higher DOFS is driven by the more positive TC in the afternoon in July, while in the nighttime the TC is closer to zero that leads to much lower DOFS. As it approaches the winter season, from October to December, the diurnal cycle of TC gradually become stronger, which shifts from positive in the daytime to negative in the nighttime. The changes are basically driven by the faster warming or cooling properties of the land compared to the atmosphere. Fortunately, both situations favor the detection of NH_3 using thermal infrared and lead to the high DOFSs in both the daytime and nighttime in both October and December.

The short lifetime of NH_3 of hours to days means that the NH_3 concentration is highly concentrated in the planetary boundary layer (PBL) around the source region. This is also illustrated by the significant higher concentration below 800 hPa in the a priori NH_3 profiles (**Figure 3**). As a result, observation of NH_3 from thermal infrared has high sensitivity closer to the surface compared to relatively longer-lived air pollutant such as carbon monoxide. The vertical sensitivities of FY-GeoAIR NH_3 retrievals are shown in **Figure 7** for the three representative regions. We can see the diurnal AK values peak at the surface layer for North China Plain for all months, especially for October and December, due to the high NH_3 concentration and favorable TC changes. In July, the nighttime sensitivity is significantly reduced in the surface layers. In North India, the bottom layers sensitivity gets to the highest at mid-night of October and December due to highly negative TC. In July, the TC closing to zeros leads to much lower AK values in North India. In Mongolia, the low background NH_3 concentration means the AK values are low over all vertical layers. The small changes in DOFS are primarily driven by the diurnal change of TC in this case. Overall, the NH_3 retrievals using FY-GeoAIR algorithm from FY-4B/GIIRS observations show high detectivity in the surface layer, especially for source regions in North China Plain and North India.
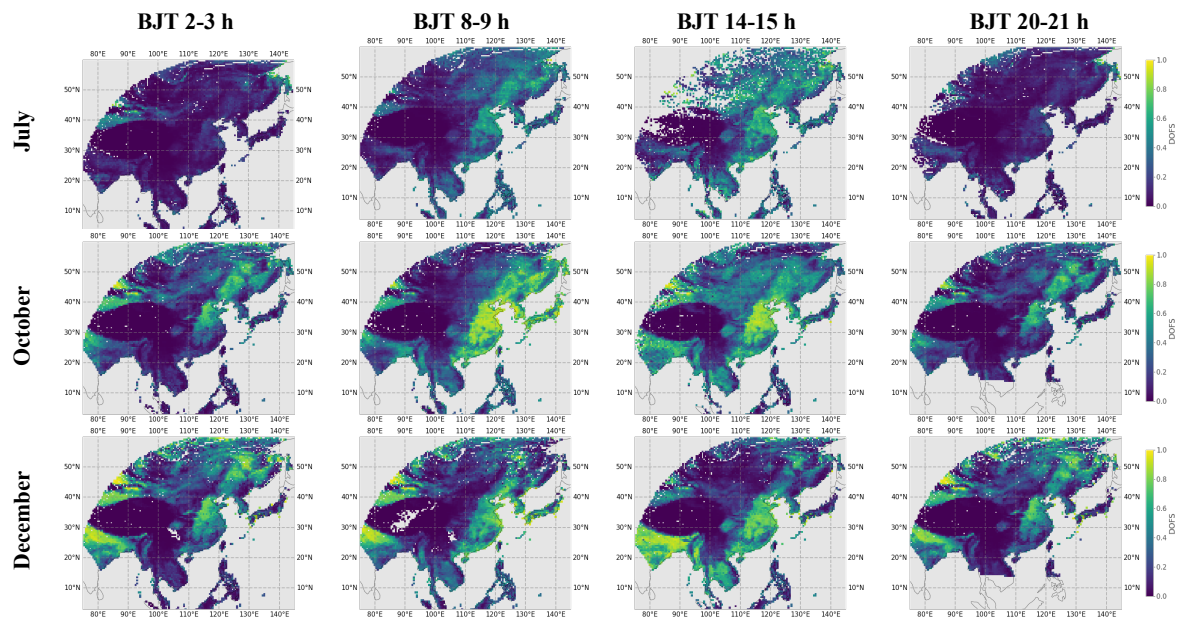
Figure 5. Spatial maps of DOFS averaged for July (summer), October (autumn), and December (winter), respectively, in 2-3h, 8-9h, 14-15h, and 20-21h in Beijing Time (BJT) to represent mid-night, early morning, afternoon, and early evening, respectively. Retrieval results using micro-window #2 (955-975 cm^{-1}) are shown. The corresponding maps for TC are presented in Supplementary Figure S2.
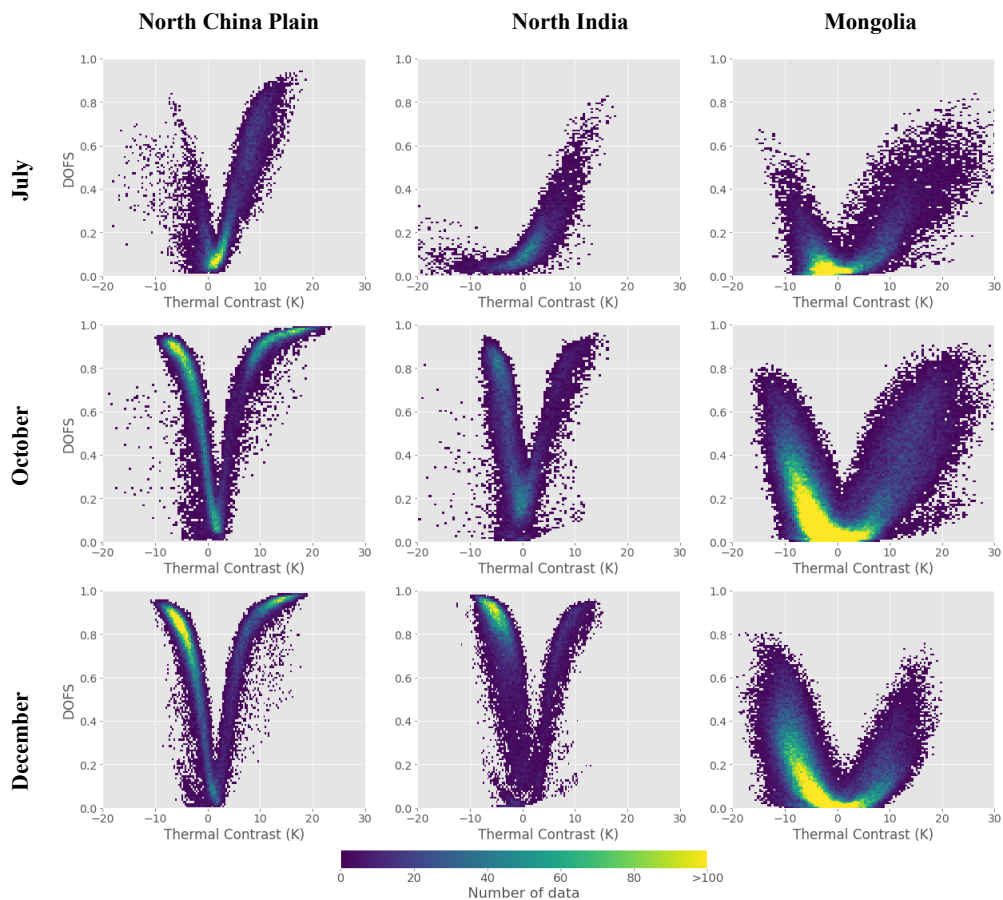
Figure 6. Scatter plots between TC and DOFS from NH₃ retrievals in North China Plain, North India, and Mongolia, respectively, for July (summer), October (autumn), and December (winter). The coverages of the three representative regions are 32°-40°N and 115°-120°E for North China Plain, 22°-27°N and 77°-87°E for North India, and 40°-50°N and 100°-110°E for Mongolia.

275
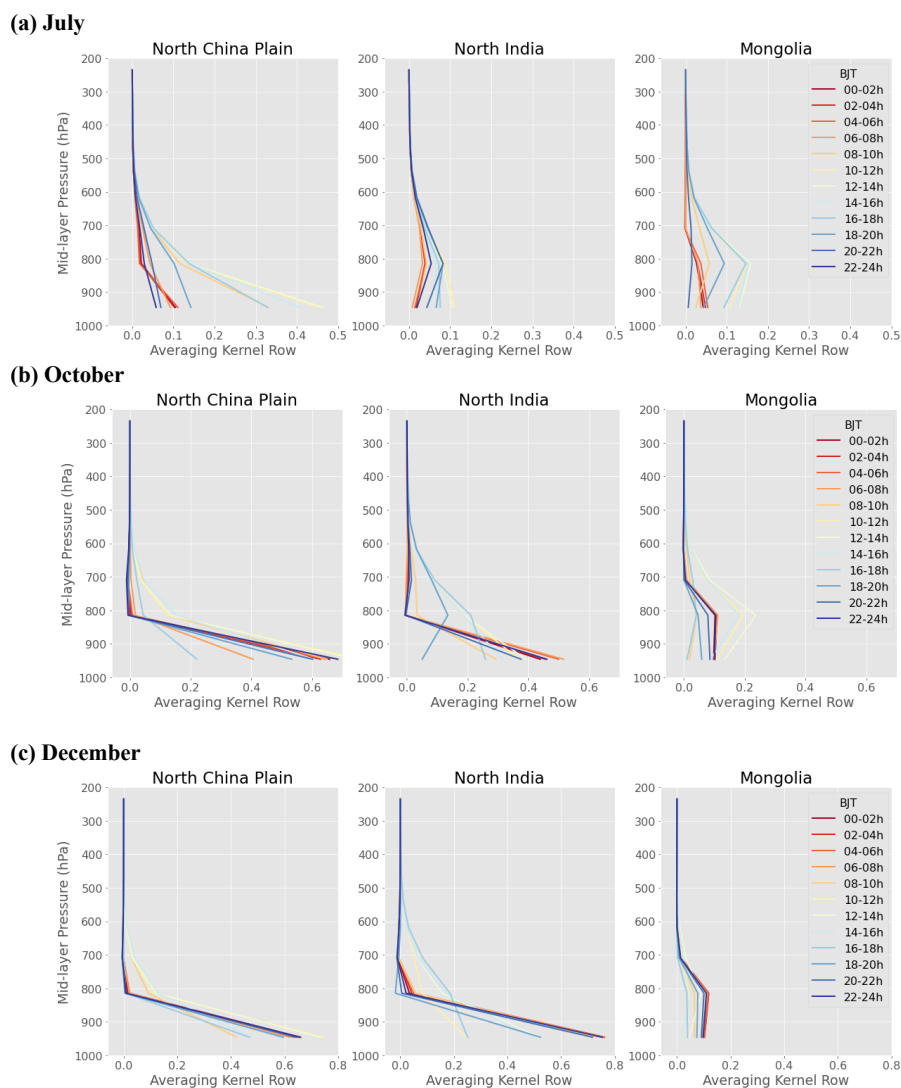
Figure 7. Averaged averaging kernel rows for the three representative regions in North China Plain, Mongolia, and North India for July (summer), October (autumn), and December (winter), respectively. The averaging kernel rows are averaged for the 2-hour duration in each measurement cycle. The coverages of the three representative regions are the same as in Figure 6.

4.3 Spatial distribution and diurnal change of NH₃ column from FY-4B/GIIRS retrievals

Spatial distribution maps of NH$_3$ columns are averaged for every 4-hour in a day and re-gridded into 0.5 by 0.5 degrees for every two months: July-August, September-October, and November-December. Before the aggregation, the post-filtered NH$_3$ retrievals are further screened by two criteria (1) DOFS>0.5 and (2) the difference between the two micro-windows is less than 2×10^{16} molec/cm^2 in order to retain retrieved columns with low uncertainty. The screened NH$_3$ retrievals from the two micro-windows are further averaged for the mapping. The results are shown in **Figures 8** and **9**. The data gaps, especially in the Tibet Plateau, are resulted from data filtering due to the low DOFS. The nighttime data in summer have been mostly filtered due to their low TC and as a result low DOFS. From these maps, obvious diurnal cycle of NH$_3$ columns can be seen from all months. North China Plain and North India, which are two agricultural intensive regions with irrigated crops and a high density of livestock, show the highest values over the region. Interestingly, the NH$_3$ columns in North India are higher than North China Plain although the bottom-up inventory in **Figure 1(a)** shows the opposite, this may be explained by the weak chemical loss and weak horizontal diffusion in North India (**Wang et al., 2020**). A more quantitative analysis of the diurnal cycle is shown in **Figure 10** for North China Plain and North India. The day-night contrast of NH$_3$ columns from IASI onboard MetopB are also indicated to check if the day-night gradients between IASI and GIIRS are consistent. Since IASI retrievals for 2022 are not available at this moment, IASI data for the past three years (2019-2021) are used.

A summary in **Clarisse et al. (2021)** concluded that the general diurnal cycle of NH$_3$ columns can be primarily explained by three possible driving factors, including the day-night difference in agriculture activities as a major source of NH$_3$, the temperature dependence of NH$_3$ emissions driven by diurnal and seasonal temperature changes, and the conversion between NH$_3$ gas and particulate driven by the day-night change of meteorological conditions. Specifically, the more significant diurnal cycle in summer (July-August) in North China Plain, capture by both GIIRS and IASI retrievals, can be explained by the higher temperature related emissions from plants and soils, and stronger daytime emissions from agricultural activities (**Meng et al., 2008**). In addition, the relatively low temperature and higher humidity contribute to the conversion from NH$_3$ to particulates that leads to a lower NH$_3$ concentration in the nighttime. In North India, unfortunately, not sufficient data are availabel in July-August after post-filtering. In September-October and November-December, the diurnal cycles become less significant compared to the summer months as the main driving factors become less important. Interestingly, the winter diurnal cycle in North China Plain and North India show opposite pattern to the diurnal cycle in summer. The slightly increase of NH$_3$ columns in the nighttime, captured by both GIIRS and IASI retrievals, may be due to the shallower nocturnal boundary layer that traps the surface emitted emissions (**Tevlin et al., 2017; Clarisse et al. 2021**). To ensure the diurnal change is not affected greatly by data quality, we also compare the GIIRS results using data with DOFS larger than 0.5 and 0.7, respectively, two thresholds that are high enough to ensure the quality of the retrievals. We can see that the difference in the diurnal cycle of NH$_3$ columns from FY-4B/GIIRS retrievals is not significant and therefore different data filters do not affect the general patterns of NH$_3$ diurnal cycle.
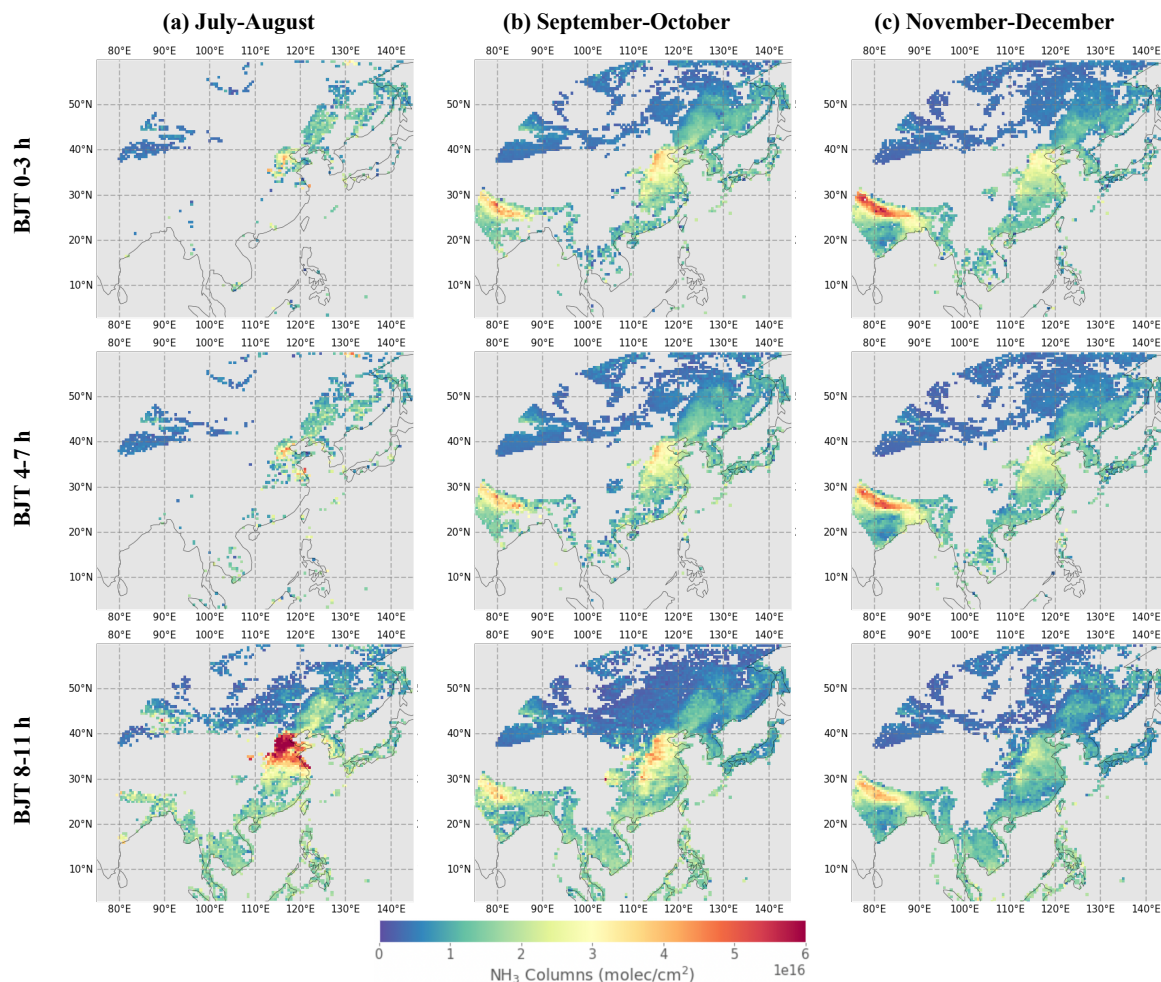
Figure 8. The monthly maps of NH$_3$ columns averaged for every four-hour (0-3 h, 4-7 h, and 8-11 h in Beijing Time) and two-month for July-August, September-October, and November-December of 2022, respectively. The NH$_3$ columns are averaged from retrievals using the two micro-windows. NH$_3$ retrievals are filtered if the difference between the two micro-window datasets is larger than 2.0×10^{16} molec/cm^2. These NH$_3$ retrievals are further filtered by DOFS>0.5 and then re-gridded into 0.5 by 0.5 degrees.

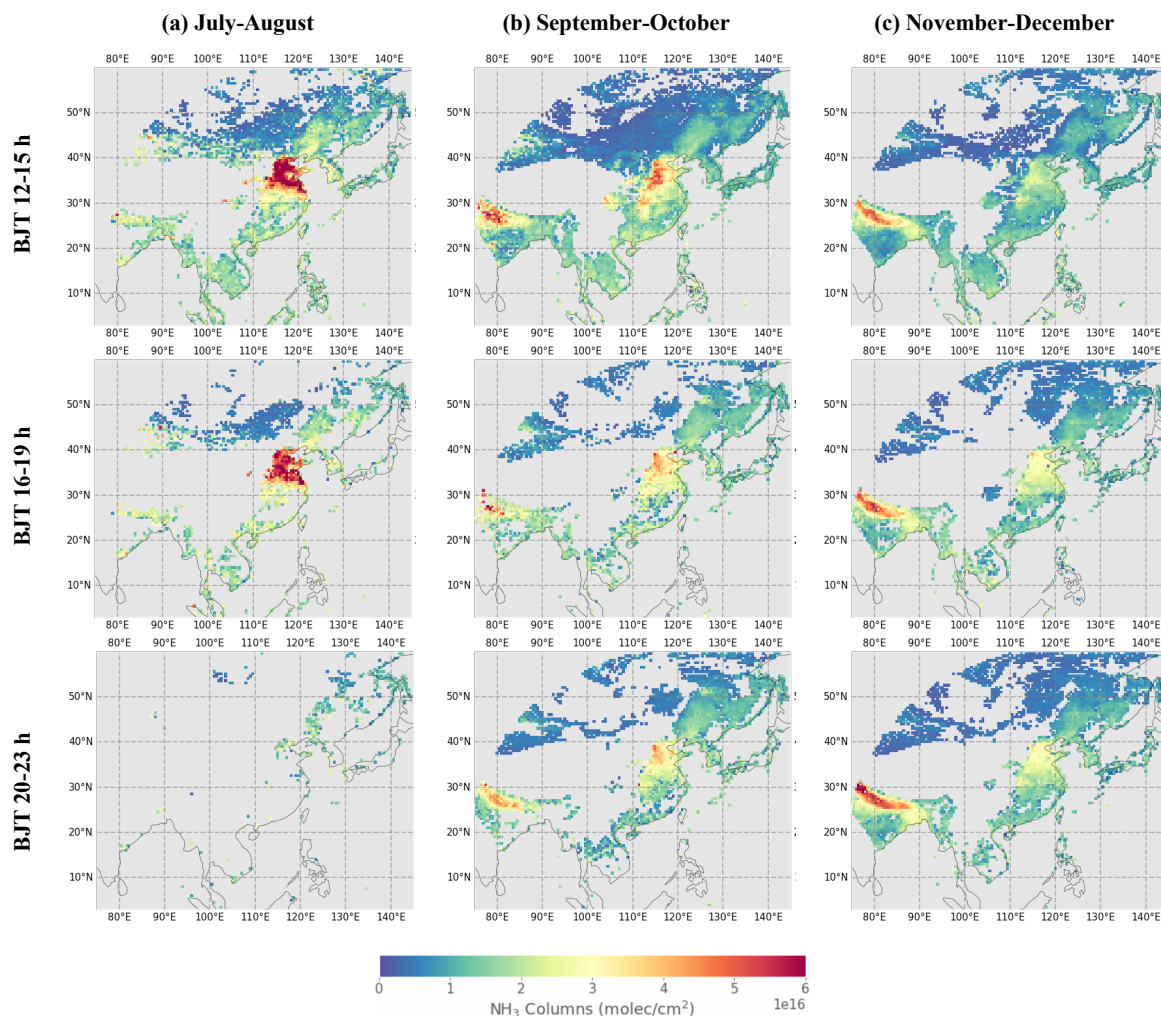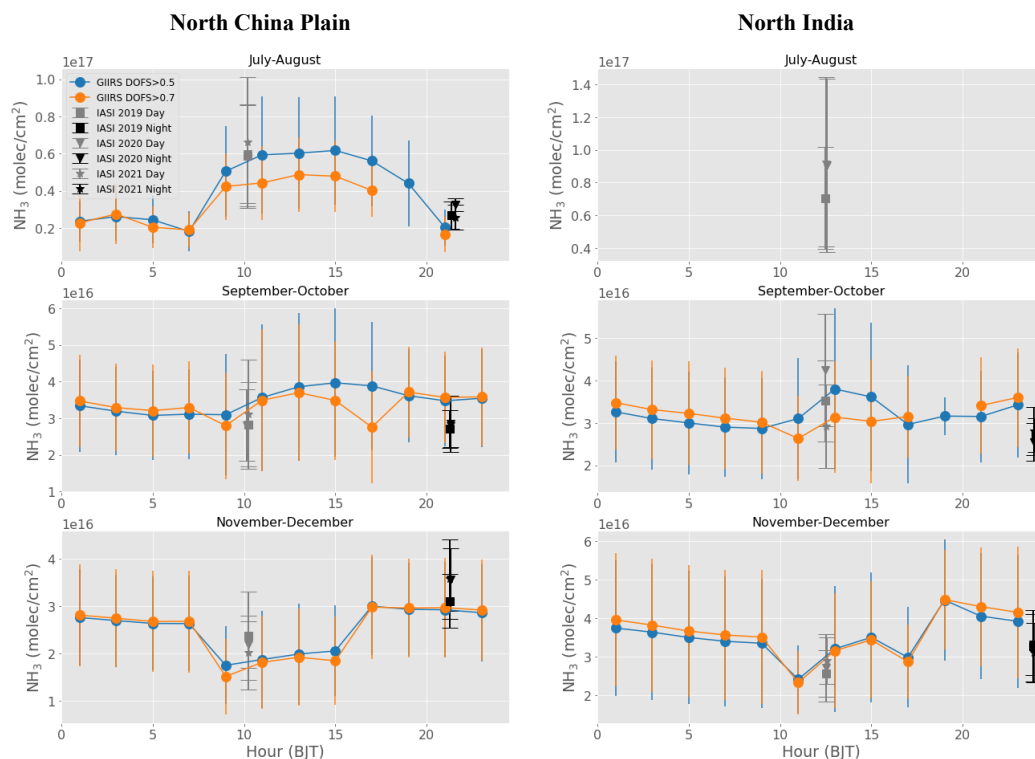Figure 9. The same as in Figure 8 but for 12-15 h, 16-19 h, and 20-23 h in Beijing Time.

Atmospheric
Measurement
Techniques
Discussions

Open Access

EGU

335

Figure 10. The diurnal cycle of NH₃ columns from FY-4B/GIIRS retrievals. The NH₃ columns are averaged from retrievals

using the two micro-windows (920-940 cm⁻¹ and 955-975 cm⁻¹) for the 2-hour duration in each measurement cycle when at

least 30 data points are available. The error bar represents one standard deviation. Retrievals are filtered if the difference

340 **between the two micro-window datasets are larger than 2.0×10^{16} molec/cm² to reduce the impact due to spectral noise.**

Diurnal cycles based on two different filtering criteria (DOFS>0.5 and DOFS>0.7) are shown simultaneously. The IASI

NH₃ column retrievals (two over-passing times in a day) are averaged values in the corresponding months for the past three

years (2019-2021). IASI NH₃ retrievals with uncertainty larger than 50% are not used. Data are averaged for daily mean,

when at least 10 data points are available, and then averaged for every two-month. The coverages of North China Plain

345 **and North India are the same as Figure 6.**

5. Discussions

5.1 Synthetic experiments for quantifying retrieval error

A synthetic experiment is carried out by (1) generating simulated synthetic spectra based on pre-determined NH_3 profiles which
350   can be regarded as the "truth", (2) adding assumed noise according to the spectra noise of FY-4B/GIIRS, and (3) applying the FY-GeoAIR algorithm to retrieve NH_3. By comparing the retrieval to the "truth", we can evaluate the performance of the retrieval algorithm and its relationship with relevant driving factors. In this experiment, the "truth" NH_3 profiles are extracted from the GEOS-CF model simulations on six representative days: July 07, August 05, September 06, October 10, November 15, and December 18 of 2022, when the available number of clear-sky observations is among the largest in the specific month. By randomly
355   sampling 500 data points for each observation cycle from the FY-4B/GIIRS clear-sky observations, we carried out 36000 simulations in total. The retrieved NH_3 columns are finally compared with the "truth" and correlated with DOFS, as shown in **Figure 11**. Simulations with DOFS less than 0.3 are not shown due to their high uncertainty and low information content extracted from the spectra measurement. The scatter plot suggests that the consistency between the retrieval and the "truth" increases when the DOFS becomes larger. For DOFS>0.5, the RMSE of the retrieval is about $1.67×10^{16}$ molec/cm^2, while for DOFS>0.7, the
360   RMSE reduces to $1.37×10^{16}$ molec/cm^2, representing error for a single retrieval. Since the retrieved NH_3 columns have a monthly mean between $2.0×10^{16}$ and $6.0×10^{16}$ molec/cm^2 as shown in **Figure 10**, this synthetic experiment results indicate that the retrieval error is on average between 23% and 68% for a single retrieval when DOFS>0.7. On the other hand, when an ensemble mean (e.g., monthly mean) of NH_3 columns is derived, the resulting error for the mean can be much smaller (reduced by a factor of sqrt(N) where N is the number of observations) when a large number of observations is available.

365
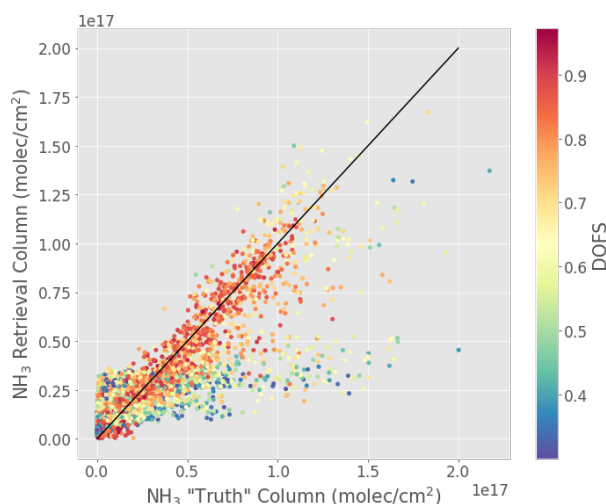
Figure 11. Comparison of retrieval and the "truth" NH_3 columns from the synthetic experiment. The retrieved NH_3 columns are based on simulated spectra generated based on pre-determined NH_3 profiles ("truth"). The data points have been filtered by DOFS>0.3 and are color-coded by the corresponding DOFS value. The RMSE of the retrieved NH_3 columns relative to the "truth" is about $1.67×10^{16}$ molec/cm^2 for DOFS>0.5 and $1.37×10^{16}$ molec/cm^2 for DOFS>0.7.

370

Atmospheric
Measurement
Techniques
Discussions

5.2 The impact of vertical shape on NH₃ retrievals

Since the observation of infrared sounder is not equally sensitive to NH_3 abundance in every layer, setting an appropriate a priori NH_3 in the retrieval algorithm is important. Extra retrieval error may be introduced if the profile is far from the truth. This is because the perturbation by the observed spectra on the sensitive layers may propagate into other layers with less sensitivity. Previous study by **Whitburn et al. (2016)** has shown that the difference in the a priori NH_3 profile is not causing significant bias in retrievals using polar orbiting satellite retrievals. Here we carried out a simple experiment to examine the impact of different vertical shape of a priori NH_3 on the retrieved columns. The a priori profiles used in the retrieval algorithm are generated by perturbing the PBL portions of the a priori, where NH_3 is concentrated, used in FY-4B/GIIRS by 2 and 0.5 times, respectively, as shown in **Figure 12(a)**. These perturbed profiles are uniformly scaled so that the total columns equal to the original a priori column. We used these profiles for the retrieval on the six representative days, as in the synthetic experiment described in **Section 6.1,** in the North China Plain. The retrievals based on perturbed profiles are then compared with original retrievals, shown in **Figure 12(b)** and **(c)**. The results show that the mean and standard deviation of the fractional error are 1.0% and 9.65%, respectively, for the reduced PBL excess profile, and 0.9% and 7.6%, respectively, for the enhanced PBL excess profile. Fortunately, there are no large systematic bias and the averaged error is within 10% in our cases of profiles differ by a factor of 2.
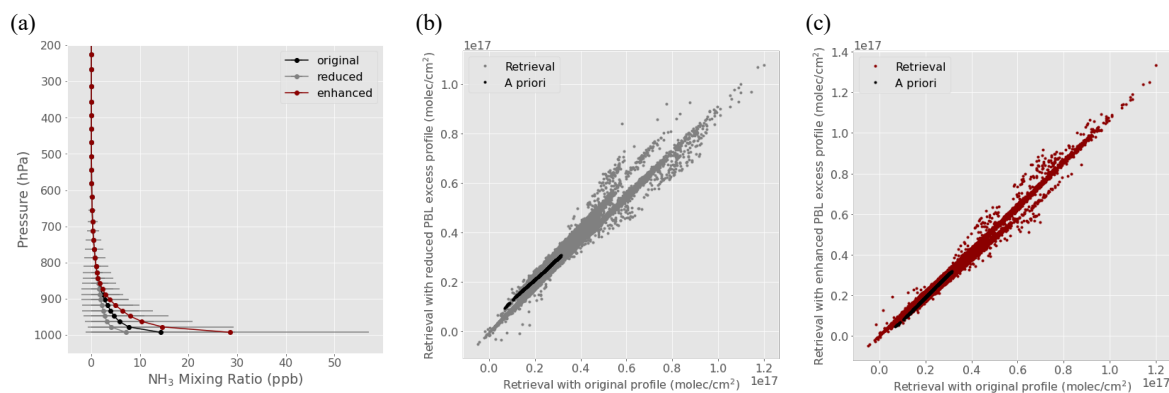
Figure 12. Comparison of retrieval results of NH₃ columns using different a priori NH₃ profiles. (a) The NH₃ a priori profile with reduced PBL excess by 50% and enhanced PBL excess by 2 times; (b) The comparison of the retrieved NH₃ column using the reduced PBL excess profile. The mean of the fractional error is 1.0% while the standard deviation is 9.6%; (c) The comparison of retrieved NH₃ column with enhanced PBL excess profile. The mean of the fractional error is 0.9% and the standard deviation is 7.6%.

Atmospheric
Measurement
Techniques
Discussions

6. Conclusions

In this study, we present an NH$_3$ retrieval algorithm based on the optimal estimation method for FY-4B/GIIRS. The DOFS and AK matrix produced from the retrieval algorithm are examined to evaluate the information content and vertical sensitivities in constraining the diurnal cycle of NH$_3$ in East Asia. Our retrievals are carried out using two different NH$_3$ absorption micro-windows

400   (920-940 cm^{-1} and 955-975 cm^{-1}), and their retrieval difference infers the impact of spectral noise on the NH$_3$ retrieval. Retrieval results using FY-4B/GIIRS spectra from July to December 2022 show that (1) the two NH$_3$ retrieval datasets using different micro-windows are highly consistent, with a correlation coefficient of 0.81 and root-mean-square-error of 3.2×10^{15} molec/cm^2 when DOFS>0.5, and no large systematic bias is observed, suggesting that the difference in the NH$_3$ retrievals is mainly originated from the impact of spectral random noise; (2) the detection sensitivity, as quantified by the AK matrix, peaks in the lowest 2 km

405   atmospheric layers, which facilitates the observation of emission sources in the PBL; (3) the DOFS and TC are highly correlated, resulting in a typical "butterfly" shape, showing that the DOFS increases when the TC becomes either more positive or more negative; (4) the diurnal cycle of NH$_3$ columns from FY-4B/GIIRS show significant diurnal cycle in summer (July-August) in North China Plain, in good agreement with the day-night gradient from the collocating IASI retrievals. The weak and moderate diurnal cycles in two important source regions of North China Plain and North India in September-October and November-

410   December are also presented from both FY-4B/GIIRS and IASI retrievals. This study demonstrates the capability of GIIRS in observing the diurnal NH$_3$ changes in East Asia, making it a unique dataset for quantifying NH$_3$ emissions and depositions and evaluating strategies for managing anthropogenic sources of NH$_3$ in Asia.

As the world's first geostationary infrared sounder, GIIRS instruments onboard FY-4A and FY-4B provide unique hyperspectral thermal infrared observations to quantify the diurnal change of atmospheric composition in East Asia. Other existing and in

415   planning geostationary missions include South Korea's Geostationary Environment Monitoring Spectrometer (GEMS) launched in Feb. 2020 to measure air quality in Asia using ultraviolet and visible bands (**Kim et al., 2020**), ESA's Sentinel-4 mission onboard the Meteosat Third Generation Sounder platform that consists of the thermal InfaRed Sounder (IRS) that will measure profiles of temperature, humidity, and atmospheric composition, and the Ultraviolet Visible Near-infrared (UVN) spectrometer that will monitor air quality trace gases and aerosols in Europe (**Ingmann et al., 2012; Holmlund et al., 2021**), and NASA's Tropospheric

420   Emissions: Monitoring of Pollution (TEMPO) that will observe air quality in North America (**Zoogman et al., 2017**). These GEO missions form a global network that enables diurnal observation to cover global important emission sources, which will significantly enhance local and global air quality and climate research.

425

Atmospheric
Measurement
Techniques
Discussions

Data availability

The sample NH_3 retrieval data from FY-4B/GIIRS in this study are publicly available from the Peking University Open Research Data Platform at https://opendata.pku.edu.cn/dataverse/FYGEOAIR; The full retrieval dataset (total data size larger than 150G) is
430 available from the corresponding author upon request. FY-4B/GIIRS Level 1 data are publicly available from the FengYun Satellite Data Center at http://satellite.nsmc.org.cn/portalsite/default.aspx; The surface emissivity datasets are downloaded from the Global Infrared Land Surface Emissivity: UW-Madison Baseline Fit Emissivity Database at https://cimss.ssec.wisc.edu/iremis/; The ECMWF ERA5 reanalysis datasets are available from the Copernicus Climate Data Store at https://cds.climate.copernicus.eu/; The ECMWF atmospheric composition datasets are available from the Copernicus Atmosphere Data Store at
435 https://ads.atmosphere.copernicus.eu/. NH_3 simulation data from GEOS-CF is downloaded from https://gmao.gsfc.nasa.gov/weather_prediction/GEOS-CF/data_access/. IASI is a joint mission of EUMETSAT and the Centre National d'Etudes Spatiales (CNES, France). The authors acknowledge the AERIS data infrastructure for providing access to the IASI data in this study, ULB-LATMOS for the development of the retrieval algorithms. IASI NH_3 retrievals are available from https://iasi.aeris-data.fr/nh3/.

Author contribution

445 Z.Z. designed the study, developed the forward model and retrieval codes, carried out the experiments and results analysis, and prepared the manuscript. L.L. and C.Q. provided guidance on using the FY-4B/GIIRS L1 spectra data and carried out experiments related to spectra uncertainty analysis. All authors reviewed the manuscript.

Competing interest

The authors declare that they have no conflict of interest.
450

References

455   Abbatt, J. P. D., Benz, S., Cziczo, D. J., Kanji, Z., Lohmann, U., and Mohler, O.: Solid ammonium sulfate aerosols as ice nuclei: A pathway for cirrus cloud formation, Science, 313, 1770–1773, https://doi.org/10.1126/science.1129726, 2006.

Aneja, V. P., Roelle, P. A., Murray, G. C., Southerland, J., Erisman, J. W., Fowler D., Asman, W. A. H., and Patni N.: Atmospheric nitrogen compounds: II. Emissions, transport, transformation, deposition and assessment, Atmos. Environ., 35, 1903–1911, 2001.

Bauduin, S., Clarisse, L., Theunissen, M., George, M., Hurtmans, D., Clerbaux, C., and Coheur, P.-F.: IASI's sensitivity to near-surface carbon monoxide (CO): Theoretical analyses and retrievals on test cases, J. Quant. Spectrosc. Ra., 189, 428–440,
460   https://doi.org/10.1016/j.jqsrt.2016.12.022, 2017.

Beer, R., Shephard, M. W., Kulawik, S. S., Clough, S. A., Eldering, A., Bowman, K. W., Sander, S. P., Fisher, B. M., Payne, V. H., Luo, M., Osterman, G. B., and Worden, J. R.: First satellite observations of lower tropospheric ammonia and methanol, Geophys. Res. Lett., 35, L09801,https://doi.org/10.1029/2008GL033642, 2008.

Clarisse, L., Clerbaux, C., Dentener, F., Hurtmans, D., and Coheur, P.-F.: Global ammonia distribution derived from infrared
465   satellite observations, Nat. Geosci., 2, 479–483, https://doi.org/10.1038/ngeo551, 2009.

Clarisse, L., Shephard, M., Dentener, F., Hurtmans, D., Cady- Pereira, K., Karagulian, F., Van Damme, M., Clerbaux, C., and Coheur, P.-F.: Satellite monitoring of ammonia: A case study of the San Joaquin Valley, J. Geophys. Res., 115, D13302, https://doi.org/10.1029/2009JD013291, 2010.

Clarisse, L., Van Damme, M., Hurtmans, D., Franco, B., Clerbaux, C., and Coheur, P. F.: The diel cycle of NH3 observed from
470   the FY-4A Geostationary Interferometric Infrared Sounder (GIIRS), Geophys. Res. Lett., 48, e2021GL093010, https://doi.org/10.1029/2021GL093010, 2021.

Clough, S. A., M. W. Shephard, E. J. Mlawer, J. S. Delamere, M. J. Iacono, K. Cady-Pereira, S. Boukabara, and P. D. Brown, Atmospheric radiative transfer modeling: a summary of the AER codes, Short Communication, J. Quant. Spectrosc. Radiat. Transfer, 91, 233-244, 2005.

475   Clough, S. A., Shephard, M. W., Worden, J., Brown, P. D., Worden, H. M., Luo, M., Rodgers, C. D., Rinsland, C. P., Goldman, A., and Brown, L.: Forward model and Jacobians for tropospheric emission spectrometer retrievals, IEEE T. Geosci. Remote, 44, 1308–1323, 2006.

Coheur, P.-F., Clarisse, L., Turquety, S., Hurtmans, D., and Clerbaux, C.: IASI measurements of reactive trace species in biomass burning plumes, Atmos. Chem. Phys., 9, 5655–5667, https://doi.org/10.5194/acp-9-5655-2009, 2009.

480   ECMWF, 2022, CAMS global inversion-optimised greenhouse gas fluxes and concentrations, available at: https://ads.atmosphere.copernicus.eu/cdsapp#!/dataset/cams-global-greenhouse-gas-inversion

Erisman, J. W., Galloway, J. N., Seitzinger, S., Bleeker, A., Dise, N. B., Petrescu, A. M. R., Leach, A. M., and de Vries, W.: Consequences of human modification of the global nitrogen cycle, Philos. Trans. R. Soc. B-Biol. Sci., 368, doi:10.1098/rstb.2013.0116, 2013.

485   Fowler, D., Coyle, M., Skiba, U., Sutton, M. A., Cape, J. N., Reis, S., Sheppard, L. J., Jenkins, A., Grizzetti, B., Galloway, J. N., Vitousek, P., Leach, A., Bouwman, A. F., Butterbach-Bahl, K., Dentener, F., Stevenson, D., Amann, M., and Voss, M.: The global nitrogen cycle in the twenty-first century, Philos. Trans. R. Soc. B-Biol. Sci., 368, 20130164, doi:10.1098/rstb.2013.0164, 2013.

Hersbach, H., Bell, B., Berrisford, P., Hirahara, S., Horányi, A., Muñoz-Sabater, J., Nicolas, J., Peubey, C., Radu, R., Schepers, D., Simmons, A., Soci, C., Abdalla, S., Abellan, X., Balsamo, G., Bechtold, P., Biavati, G., Bidlot, J., Bonavita, M., De Chiara,
490   G., Dahlgren, P., Dee, D., Diamantakis, M., Dragani, R., Flemming, J., Forbes, R., Fuentes, M., Geer, A., Haimberger, L., Healy, S., Hogan, R. J., Hólm, E., Janisková, M., Keeley, S., Laloyaux, P., Lopez, P., Lupu, C., Radnoti, G., de Rosnay, P., Rozum, I., Vamborg, F., Villaume, S., and Thépaut, J. N.: The ERA5 global reanalysis, Q. J. Roy. Meteor. Soc., 146, 1999–2049, https://doi.org/10.1002/qj.3803, 2020.

Holmlund, K., Grandell, J., Schmetz, J., Stuhlmann, R., Bojkov, B., Munro, R., Lekouara, M., Coppens, D., Viticchie, B., August,
495   T., Theodore, B., Watts, P., Dobber, M., Fowler, G., Bojinski, S., Schmid, A., Salonen, K., Tjemkes, S., Aminou, D., and Blythe,

P.: Meteosat Third Generation (MTG): Continuation and innovation of observations from geostationary orbit, B. Am. Meteorol. Soc., 102, E990–E1015, https://doi.org/10.1175/BAMS-D-19-0304.1, 2021.

Hurtmans, D., Coheur, P.-F., Wespes, C., Clarisse, L., Scharf, O., Clerbaux, C., Hadji-Lazaro, J., George, M., and Turquety, S.: FORLI radiative transfer and retrieval code for IASI, J. Quant. Spectrosc. Ra., 113, 1391–1408, https://doi.org/10.1016/j.jqsrt.2012.02.036, 2012.

Ingmann, P., B. Veihelmann, J. Langen, D. Lamarre, H. Stark, and G. B. Courrèges- Lacoste: Requirements for the GMES atmosphere service and ESA's implementation concept: Sentinels-4/-5 and -5p. Remote Sens. Environ., 120, 58–69, https://doi.org/10.1016/j.rse.2012.01.023, 2012.

Isaksen, I. S. A., Granier, C., Myhre, G., Berntsen, T. K., Dalsoren, S. B., Gauss, M., Klimont, Z., Benestad, R., Bousquet, P., Collins, W., Cox, T., Eyring, V., Fowler, D., Fuzzi, S., Jockel, P., Laj, P., Lohmann, U., Maione, M., Monks, P., Prevot, A. S. H., Raes, F., Richter, A., Rognerud, B., Schulz, M., Shindell, D., Stevenson, D. S., Storelvmo, T., Wang, W. C., van Weele, M., Wild, M., and Wuebbles, D.: Atmospheric composition change: Climate-Chemistry interactions, Atmos. Environ., 43, 5138–5192, doi:10.1016/j.atmosenv.2009.08.003, 2009.

Galloway, J. N., Dentener, F. J., Capone, D. G., Boyer, E. W., Howarth, R. W., Seitzinger, S. P., Asner, G. P., Cleveland, C. C., Green, P. A., and Holland, E. A.: Nitrogen cycles: past, present, and future, Biogeochemistry, 70, 153–226, 2004.

Li, J., Menzel, W. P., Schmit, T. J., and Schmetz J.: Applications of Geostationary Hyperspectral Infrared Sounder Observations: Progress, Challenges, and Future Perspectives, Bull. Am. Meteorol. Soc., 103, 12 (2022), E2733-E2755, https://doi.org/10.1175/BAMS-D-21-0328.1, 2022

Li, M., Zhang, Q., Kurokawa, J.-I., Woo, J.-H., He, K., Lu, Z., Ohara, T., Song, Y., Streets, D. G., Carmichael, G. R., Cheng, Y., Hong, C., Huo, H., Jiang, X., Kang, S., Liu, F., Su, H., and Zheng, B.: MIX: a mosaic Asian anthropogenic emission inventory under the international collaboration framework of the MICS-Asia and HTAP, Atmos. Chem. Phys., 17, 935-963, doi:10.5194/acp-17-935-2017, 2017.

Keller, C. A., Knowland, K. E., Duncan, B. N., Liu, J., Anderson, D. C., Das, S., Lucchesi, R. A., Lundgren, E. W., Nicely, J. M., Nielsen, E., Ott, L. E., Saunders, E., Strode, S. A., Wales, P. A., Jacob, D. J., and Pawson, S.: Description of the NASA GEOS Composition Forecast Modeling System GEOS-CF v1.0, J. Adv. Model. Earth Sy., 13, e2020MS002413, https://doi.org/10.1029/2020MS002413, 2021

Kim, J., Jeong, U., Ahn, M. H., Kim, J. H., Park, R. J., Lee, H., Song, C. H., Choi, Y. S., Lee, K. H., Yoo, J. M., Jeong, M. J., Park, S. K., Lee, K. M., Song, C. K., Kim, S. W., Kim, Y. J., Kim, S. W., Kim, M., Go, S., Liu, X., Chance, K., Miller, C. C., Al-Saadi, J., Veihelmann, B., Bhartia, P. K., Torres, O., Abad, G. G., Haffner, D. P., Ko, D. H., Lee, S. H., Woo, J. H., Chong, H., Park, S. S., Nicks, D., Choi, W. J., Moon, K. J., Cho, A., Yoon, J., Kim, S. kyun, Hong, H., Lee, K., Lee, H., Lee, S., Choi, M., Veefkind, P., Levelt, P. F., Edwards, D. P., Kang, M., Eo, M., Bak, J., Baek, K., Kwon, H. A., Yang, J., Park, J., Han, K. M., Kim, B. R., Shin, H. W., Choi, H., Lee, E., Chong, J., Cha, Y., Koo, J. H., Irie, H., Hayashida, S., Kasai, Y., Kanaya, Y., Liu, C., Lin, J., Crawford, J. H., Carmichael, G. R., Newchurch, M. J., Lefer, B. L., Herman, J. R., Swap, R. J., Lau, A. K. H., Kurosu, T. P., Jaross, G., Ahlers, B., Dobber, M., McElroy, C. T. and Choi, Y.: New era of air quality monitoring from space: Geostationary environment monitoring spectrometer (GEMS), Bull. Am. Meteorol. Soc., 101(1), E1–E22, https://doi.org/10.1175/BAMS-D-18-0013.1, 2020.

Meng, Z., Xu, X., Lin, W., Ge, B., Xie, Y., Song, B., Jia, S., Zhang, R., Peng, W., Wang, Y., Cheng, H., Yang, W., and Zhao, H.: Role of ambient ammonia in particulate ammonium formation at a rural site in the North China Plain, Atmos. Chem. Phys., 18, 167–184, https://doi.org/10.5194/acp-18-167-2018, 2018.

Monks, P. S., Granier, C., Fuzzi, S., Stohl, A., Williams, M. L., Akimoto, H., Amann, M., Baklanov, A., Baltensperger, U., Bey, I., Blake, N., Blake, R. S., Carslaw, K., Cooper, O. R., Dentener, F., Fowler, D., Fragkou, E., Frost, G. J., Generoso, S., Ginoux, P., Grewe, V., Guenther, A., Hansson, H. C., Henne, S., Hjorth, J., Hofzumahaus, A., Huntrieser, H., Isaksen, I. S. A., Jenkin, M. E., Kaiser, J., Kanakidou, M., Klimont, Z., Kulmala, M., Laj, P., Lawrence, M. G., Lee, J. D., Liousse, C., Maione, M., McFiggans, G., Metzger, A., Mieville, A., Moussiopoulos, N., Orlando, J. J., O'Dowd, C. D., Palmer, P. I., Parrish, D. D., Petzold, A., Platt, U., Poeschl, U., Prevot, A. S. H., Reeves, C. E., Reimann, S., Rudich, Y., Sellegri, K., Steinbrecher, R., Simpson, D., ten Brink, H., Theloke, J., van der Werf, G. R., Vautard, R., Vestreng, V., Vlachokostas, C., and von Glasow, R.: Atmospheric composition change – global and regional air quality, Atmos. Environ., 43, 5268–5350, doi:10.1016/j.atmosenv.2009.08.021, 2009.

Natraj, V., Luo, M., Blavier, J.-F., Payne, V. H., Posselt, D. J., Sander, S. P., Zeng, Z.-C., Neu, J. L., Tremblay, D., Wu, L., Roman, J. A., Wu, Y.-H., and Dorsky, L. I.: Simulated multispectral temperature and atmospheric composition retrievals for the JPL GEO-IR Sounder, Atmos. Meas. Tech., 15, 1251–1267, https://doi.org/10.5194/amt-15-1251-2022, 2022.

545 Paerl, H. W., Gardner, W. S., McCarthy, M. J., Peierls, B. L., and Wilhelm, S. W.: Algal blooms: Noteworthy nitrogen, Science, 346, 175–175, https://doi.org/10.1126/science.346.6206.175-a, 2014.

Rodgers, C. D.: Inverse Methods for Atmospheric Sounding: Theory and Practice, World Scientific, Singapore, 2000.

Seemann, S. W., Borbas, E. E., Knuteson, R. O., Stephenson, G. R., and Huang, H.-L.: Development of a Global Infrared Land Surface Emissivity Database for Application to Clear Sky Sounding Retrievals from Multi-spectral Satellite Radiance 550 Measurements, J. Appl. Meteorol. Clim., 47, 108–123, https://doi.org/10.1175/2007JAMC1590.1, 2008.

Seinfeld, J. H. and Pandis, S. N.: Atmospheric Chemistry and Physics: From Air Pollution to Climate Change, John Wiley, New York, 2006.

Shephard, M. W., Cady-Pereira, K. E., Luo, M., Henze, D. K., Pinder, R. W., Walker, J. T., Rinsland, C. P., Bash, J. O., Zhu, L., Payne, V. H., and Clarisse, L.: TES ammonia retrieval strategy and global observations of the spatial and seasonal variability of 555 ammonia, Atmos. Chem. Phys., 11, 10743–10763, doi:10.5194/acp-11-10743-2011, 2011.

Shephard, M. W., Dammers, E., Cady-Pereira, K. E., Kharol, S. K., Thompson, J., Gainariu-Matz, Y., Zhang, J., McLinden, C. A., Kovachik, A., Moran, M., Bittman, S., Sioris, C. E., Griffin, D., Alvarado, M. J., Lonsdale, C., Savic-Jovcic, V., and Zheng, Q.: Ammonia measurements from space with the Cross-track Infrared Sounder: characteristics and applications, Atmos. Chem. Phys., 20, 2277–2302, https://doi.org/10.5194/acp-20-2277-2020, 2020.

560 Tevlin, A. G., Li, Y., Collett, J. L., McDuffie, E. E., Fischer, E. V., and Murphy, J. G.: Tall Tower Vertical Profiles and Diurnal Trends of Ammonia in the Colorado Front Range, J. Geophys. Res.-Atmos., 122, 12468–12487, https://doi.org/10.1002/2017JD026534, 2017.

Someya, Y., Imasu, R., Shiomi, K., and Saitoh, N.: Atmospheric ammonia retrieval from the TANSO-FTS/GOSAT thermal infrared sounder, Atmos. Meas. Tech., 13, 309–321, https://doi.org/10.5194/amt-13-309-2020, 2020.

565 Van Damme, M., Whitburn, S., Clarisse, L., Clerbaux, C., Hurtmans, D., and Coheur, P.-F.: Version 2 of the IASI NH3 neural network retrieval algorithm: near-real-time and reanalysed datasets, Atmos. Meas. Tech., 10, 4905–4914, https://doi.org/10.5194/amt-10-4905-2017, 2017.

Van Damme, M., Clarisse, L., Whitburn, S., Hadji-Lazaro, J., Hurtmans, D., Clerbaux, C., and Coheur, P.-F.: Industrial and agricultural ammonia point sources exposed, Nature, 564, 99–103, https://doi.org/10.1038/s41586-018-0747-1, 2018.

570 Van Damme, M., Clarisse, L., Franco, B., Sutton, M. A., Erisman, J. W., Kruit, R. J. W., van Zanten, M., Whitburn, S., Hadji-Lazaro, J., Hurtmans, D., Clerbaux, C., and Coheur, P. F.: Global, regional and national trends of atmospheric ammonia derived from a decadal (2008–2018) satellite record, Environ. Res. Lett., https://doi.org/10.1088/1748-9326/abd5e0, 2020.

Wang, T., Song, Y., Xu, Z., Liu, M., Xu, T., Liao, W., Yin, L., Cai, X., Kang, L., Zhang, H., and Zhu, T.: Why is the Indo-Gangetic Plain the region with the largest NH3 column in the globe during pre-monsoon and monsoon seasons?, Atmos. Chem. Phys., 20, 575 8727–8736, https://doi.org/10.5194/acp-20-8727-2020, 2020.

Warner, J. X., Wei, Z., Strow, L. L., Dickerson, R. R., and Nowak, J. B.: The global tropospheric ammonia distribution as seen in the 13-year AIRS measurement record, Atmos. Chem. Phys., 16, 5467–5479, https://doi.org/10.5194/acp-16-5467-2016, 2016.

Warner, J. X., Dickerson, R. R., Wei, Z., Strow, L. L., Wang, Y., and Liang, Q.: Increased atmospheric ammonia over the world's major agricultural areas detected from space, Geophys. Res. Lett., 44, 2875–2884, https://doi.org/10.1002/2016gl072305, 2017.

580 Whitburn, S., Van Damme, M., Clarisse, L., Bauduin, S., Heald, C. L., Hadji-Lazaro, J., Hurtmans, D., Zondlo, M. A., Clerbaux, C., and Coheur, P.-F.: A flexible and robust neural network IASI- NH3 retrieval algorithm, J. Geophys. Res.-Atmos., 121, 6581–6599, https://doi.org/10.1002/2016jd024828, 2016.

Yang, J., Zhang, Z., Wei, C., Lu, F., and Guo, Q.: Introducing the new generation of Chinese geostationary weather satellites, Fengyun-4, B. Am. Meteorol. Soc., 98, 1637–1658, https://doi.org/10.1175/BAMS-D-16-0065.1, 2017.

585 Zeng, Z.-C., Zhang, Q., Natraj, V., Margolis, J. S., Shia, R.-L., Newman, S., Fu, D., Pongetti, T. J., Wong, K. W., Sander, S. P., Wennberg, P. O., and Yung, Y. L.: Aerosol scattering effects on water vapor retrievals over the Los Angeles Basin, Atmos. Chem. Phys., 17, 2495–2508, https://doi.org/10.5194/acp-17-2495-2017, 2017.

590   Zeng, Z.-C., Natraj, V., Xu, F., Chen, S., Gong, F.-Y., Pongetti, T. J., Sung, K., Toon, G., Sander, S. P., and Yung, Y. L.: GFIT3: a full physics retrieval algorithm for remote sensing of greenhouse gases in the presence of aerosols, Atmos. Meas. Tech., 14, 6483–6507, https://doi.org/10.5194/amt-14-6483-2021, 2021.

Zeng, Z.-C., Lee, L., and Qi, C.: Diurnal carbon monoxide observed from a geostationary infrared hyperspectral sounder: First result from GIIRS onboard FY-4B, Atmos. Meas. Tech. Discuss. [preprint], https://doi.org/10.5194/amt-2022-305, in review, 2022.

Zhu, L., Henze, D., Bash, J., Jeong, G.-R., Cady-Pereira, K., Shephard, M., Luo, M., Paulot, F., and Capps, S.: Global evaluation of ammonia bidirectional exchange and livestock diurnal variation schemes, Atmos. Chem. Phys., 15, 12823–12843, 595   https://doi.org/10.5194/acp-15-12823-2015, 2015.

Zoogman, P., Liu, X., Suleiman, R., Pennington, W., Flittner, D., Al-Saadi, J., Hilton, B., Nicks, D., Newchurch, M., Carr, J., Janz, S., Andraschko, M., Arola, A., Baker, B., Canova, B., Miller, C. C., Cohen, R., Davis, J., Dussault, M., Edwards, D., Fishman, J., Ghulam, A., Abad, G. G., Grutter, M., Herman, J., Houck, J., Jacob, D., Joiner, J., Kerridge, B., Kim, J., Krotkov, N., Lamsal, L., Li, C., Lindfors, A., Martin, R., McElroy, C., McLinden, C., Natraj, V., Neil, D., Nowlan, C., O'Sullivan, E., Palmer, P., Pierce, 600   R., Pippin, M., Saiz-Lopez, A., Spurr, R., Szykman, J., Torres, O., Veefkind, J., Veihelmann, B., Wang, H., Wang, J., and Chance, K.: Tropospheric emissions: Monitoring of pollution (TEMPO), J. Quant. Spectrosc. Ra., 186, 17–39, https://doi.org/10.1016/j.jqsrt.2016.05.008, 2017.